Verification of a non-hydrostatic dynamical core using horizontally spectral element vertically finite difference method: 2D Aspects

Suk-Jin Choi[1),*], Francis X. Giraldo[2)], Junghan Kim[1)], and Seoleun Shin[1)]

1) Korea institute of atmospheric prediction systems, 4F., 35 Boramae-ro 5-gil, Dongjak-gu, Seoul 156-849, Korea

2) Department of Applied Mathematics, Naval Postgraduate School, 833 Dyer Road, Monterey, CA 93943, USA

April, 2014,

Submitted to *Monthly Weather Review*

*Corresponding author address: Dr. Suk-Jin Choi, Korea institute of atmospheric prediction systems, 4F., 35 Boramae-ro 5-gil, Dongjak-gu, Seoul 156-849, Korea. Email: sj.choi@kiaps.org

Report Documentation Page

Form Approved
OMB No. 0704-0188

1. REPORT DATE	2. REPORT TYPE	3. DATES COVERED
APR 2014		**00-00-2014 to 00-00-2014**

4. TITLE AND SUBTITLE
Verification of a non-hydrostatic dynamical core using horizontally spectral element vertically finite difference method: 2D Aspects

5a. CONTRACT NUMBER
5b. GRANT NUMBER
5c. PROGRAM ELEMENT NUMBER

6. AUTHOR(S)

5d. PROJECT NUMBER
5e. TASK NUMBER
5f. WORK UNIT NUMBER

7. PERFORMING ORGANIZATION NAME(S) AND ADDRESS(ES)
Naval Postgraduate School,Department of Applied Mathematics,Monterey,CA,93943

8. PERFORMING ORGANIZATION REPORT NUMBER

9. SPONSORING/MONITORING AGENCY NAME(S) AND ADDRESS(ES)

10. SPONSOR/MONITOR'S ACRONYM(S)
11. SPONSOR/MONITOR'S REPORT NUMBER(S)

12. DISTRIBUTION/AVAILABILITY STATEMENT
Approved for public release; distribution unlimited

13. SUPPLEMENTARY NOTES

14. ABSTRACT

The non-hydrostatic (NH) compressible Euler equations of dry atmosphere are solved in a simplified two dimensional (2D) slice (X-Z) framework employing a spectral element method (SEM) for the horizontal discretization and a finite difference method (FDM) for the vertical discretization. The SEM uses high-order nodal basis functions associated with Lagrange polynomials based on Gauss-Lobatto-Legendre (GLL) quadrature points. The FDM employs a third-order upwind biased scheme for the vertical flux terms and a centered finite difference scheme for the vertical derivative terms and quadrature. The Euler equations used here are in a flux form based on the hydrostatic pressure vertical coordinate, which are the same as those used in the Weather Research and Forecasting (WRF) model, but a hybrid sigma-pressure vertical coordinate is implemented in this model. We verified the model by conducting widely used standard benchmark tests: the inertia-gravity wave, rising thermal bubble, density current wave, and linear hydrostatic mountain wave. The numerical results demonstrate that the horizontally spectral element vertically finite difference model is accurate and robust. By using the 2D slice model, we effectively show that the combined spatial discretization method of the spectral element and finite difference method in the horizontal and vertical directions, respectively, offers a viable method for the development of a NH dynamical core. The present core provides a practical framework for further development of three-dimensional (3D) non-hydrostatic compressible atmospheric models.

15. SUBJECT TERMS

16. SECURITY CLASSIFICATION OF:			17. LIMITATION OF ABSTRACT	18. NUMBER OF PAGES	19a. NAME OF RESPONSIBLE PERSON
a. REPORT	b. ABSTRACT	c. THIS PAGE			
unclassified	**unclassified**	**unclassified**	**Same as Report (SAR)**	**41**	

Abstract

The non-hydrostatic (NH) compressible Euler equations of dry atmosphere are solved in a simplified two dimensional (2D) slice (X-Z) framework employing a spectral element method (SEM) for the horizontal discretization and a finite difference method (FDM) for the vertical discretization. The SEM uses high-order nodal basis functions associated with Lagrange polynomials based on Gauss-Lobatto-Legendre (GLL) quadrature points. The FDM employs a third-order upwind biased scheme for the vertical flux terms and a centered finite difference scheme for the vertical derivative terms and quadrature. The Euler equations used here are in a flux form based on the hydrostatic pressure vertical coordinate, which are the same as those used in the Weather Research and Forecasting (WRF) model, but a hybrid sigma-pressure vertical coordinate is implemented in this model. We verified the model by conducting widely used standard benchmark tests: the inertia-gravity wave, rising thermal bubble, density current wave, and linear hydrostatic mountain wave. The numerical results demonstrate that the horizontally spectral element vertically finite difference model is accurate and robust. By using the 2D slice model, we effectively show that the combined spatial discretization method of the spectral element and finite difference method in the horizontal and vertical directions, respectively, offers a viable method for the development of a NH dynamical core. The present core provides a practical framework for further development of three-dimensional (3D) non-hydrostatic compressible atmospheric models.

1. Introduction

There is a growing interest in developing highly scalable dynamical cores using numerical algorithms under petascale computers with many cores (with the goal of exascale computing just around the corner). The spectral element method (SEM) has been known as one of the most promising methods with high efficiency and accuracy (Taylor et al. 1997; Giraldo 2001; Thomas and Loft 2002). SEM is local in nature because of having a large on-processor operation count (Kelly and Graldo, 2012). The SEM achieves this high level of scalability by decomposing the physical domain into smaller pieces with a small communication stencil. Also SEM has been shown to be very attractive in achieving high-order accuracy and geometrical flexibility on the sphere (Taylor et al. 1997; Giraldo 2001; Giraldo et al. 2004).

To date, the SEM has been successfully implemented in atmospheric modeling such as in the Community Atmosphere Model – spectral element dynamical core (CAM-SE) (Thomas and Loft 2005) and the scalable spectral element Eulerian atmospheric model (SEE-AM) (Giraldo and Rosmond, 2004). These models consider the primitive hydrostatic equations on global grid meshes such as a cubed-sphere tiled with quadrilateral elements using SEM in the horizontal discretization and the finite difference method (FDM) in the vertical. The robustness of the SEM has been illustrated through three-dimensional dry dynamical test cases (Thomas and Loft 2005; Giraldo and Rosmond 2004; Giraldo 2005; Taylor et al. 2007; Lauritzen et al. 2010).

The ultimate objective of our study is to build a 3D non-hydrostatic (NH) model based on the compressible Navier-Stokes equations using the combined horizontally SEM and vertically FDM. Since testing a 3D NH model requires a huge amount of computing resources, studying the feasibility of our approach in 2D is an attractive alternatively to the

development of a fully 3D model. This is the case because a 2D slice model effectively can test the practical issues resulting from the vertical discretization and time integration, prior to the construction of a full 3D model. Although we could also discretize the vertical direction with SEM (as is proposed in Kelly and Giraldo 2012 and Giraldo et al. 2013), we choose to use a conservative flux-form finite-difference method for discretization in the vertical direction, which provides an easy way for coupling the dynamics and existing physics packages.

We have developed a dry 2D NH compressible Euler model based on SEM along the x-direction and FDM along the z-direction for this purpose. Hereafter, this is simply referred to as the 2DNH model. We adopt the governing equation formulation proposed by Skamarock and Klemp (2008) (hereafter, SK08) which is used in the Weather Research and Forecasting (WRF) Model. The Euler equations are in flux form based on the hydrostatic pressure vertical coordinate. In SK08, the terrain-following sigma-pressure coordinate is used, but here we employ a hybrid sigma-pressure vertical coordinate. Park et al. (2013) (hereafter, PK13) provides a clue for the equation set in the hybrid sigma-pressure in their appendix, in which the hybrid sigma-pressure coordinate is applied to the hydrostatic primitive equations and can be modified exactly to the sigma-pressure coordinate at the level of the actual coding implementation. Also, we built the 2DNH model using a time-split third-order Runge-Kutta (RK3) for the time discretization, which has been shown to work effectively in the WRF model. We keep the temporal discretization of the model as similar as possible to the WRF model in order to more directly the discern the differences related to the discrete spatial operators between the two models. This provides robust tools for development and verification of the 2DNH model.

In this paper, we show the feasibility of the 2DNH model by conducting conventional benchmark test cases as well as focusing on the description of the numerical scheme for the

spatial discretization. We verify the 2DNH by analyzing four test cases: the inertia-gravity wave, rising thermal bubble, density current wave, and linear hydrostatic mountain wave.

The organization of this paper is as follows. The next section describes the governing equations with a definition of the prognostic and diagnostic variables used in our model, in which we present essential changes from SK08. Section 3 contains the description of the temporal and spatial discretization including the spectral element formulation. In Sec. 4, we present the results of the 2DNH model using all four test cases. Finally in Sec. 5 we summarize the paper and propose future directions.

2. Governing equations

We adopt the governing equation formulation of SK08. Here we implement the hybrid sigma-pressure coordinate reported by PK13 which considered only the hydrostatic primitive equation. The hybrid sigma pressure coordinate is defined with $\eta \in \left[0,1\right]$ as

$$p_d = B(\eta)\left(p_s - p_t\right) + \left[\eta - B(\eta)\right]\left(p_0 - p_t\right) + p_t \tag{1}$$

where p_d is the hydrostatic pressure of dry air, $B(\eta)$ is the relative weighting of the terrain-following coordinate versus the normalized pressure coordinate, p_s, p_t, and p_0 are the hydrostatic surface pressure of dry air, the top level pressure, and a reference sea level pressure, respectively. A more detailed description of the hybrid sigma pressure coordinate can be found in the Appendix of PK13. The definition of the flux variables are

$$\left(\vec{V}_H, \mathrm{W}, \Omega, \Theta\right) = \mu_d \times \left(\vec{v}_H, \mathrm{w}, \dot{\eta}, \theta\right) \tag{2}$$

where $\vec{v}_H = \left(u, v\right)$ and w are the velocities in the horizontal and vertical directions, respectively, $\dot{\eta} \equiv \frac{\partial \eta}{\partial t}$ is the η-coordinate (contravariant) vertical velocity, θ is the

potential temperature, and μ_d is the mass of the dry air in the layers defined as

$$\mu_d(x,y,\eta,t) = \frac{\partial p_d}{\partial \eta} = \frac{\partial B(\eta)}{\partial \eta}\left(p_s - p_t\right) + \left[1 - \frac{\partial B(\eta)}{\partial \eta}\right]\left(p_0 - p_t\right). \quad (3)$$

The flux-form Euler equations for dry atmosphere are expressed as

$$\frac{\partial \vec{V}_H}{\partial t} = -\mu_d\left(\nabla_\eta \phi' + \alpha_d \nabla_\eta p' + \alpha_d' \nabla_\eta \bar{p}\right) - \nabla_\eta \phi\left(\frac{\partial p'}{\partial \eta} - \mu_d'\right) - \nabla_\eta \cdot \left(\vec{V}_H \otimes \vec{v}_H\right) - \frac{\partial\left(\Omega \vec{V}_H\right)}{\partial \eta} + F_{\vec{V}_H}, \quad (4)$$

$$\frac{\partial W}{\partial t} = g\left[\frac{\partial p'}{\partial \eta} - \mu_d'\right] - \nabla_\eta \cdot \left(\vec{V}_H W\right) - \frac{\partial\left(\Omega w\right)}{\partial \eta} + F_W, \quad (5)$$

$$\frac{\partial \mu_d'}{\partial t} = \frac{\partial}{\partial t}\left(\frac{\partial p_d'}{\partial \eta}\right) = \frac{\partial B(\eta)}{\partial \eta}\frac{\partial p_s'}{\partial t} = -\nabla_\eta \cdot \vec{V}_H - \frac{\partial \Omega}{\partial \eta}, \quad (6)$$

$$\frac{\partial \phi'}{\partial t} = -\frac{1}{\mu_d}\left[\vec{V}_H \cdot \nabla_\eta \phi + \Omega \frac{\partial \phi}{\partial \eta} - gW\right], \quad (7)$$

$$\frac{\partial \Theta}{\partial t} = -\nabla_\eta \cdot \left(\vec{V}_H \theta\right) - \frac{\partial\left(\Omega \theta\right)}{\partial \eta}, \quad (8)$$

where ϕ is the geopotential, α_d is the inverse density for dry air, and F_{V_H} and F_W represent forcing terms of the Coriolis and curvature which we ignore for simplicity. In Eqs. (4)-(8), the governing equations are described with perturbation variables such as $p = \bar{p}(\bar{z}) + p'$, $\phi = \bar{\phi}(\bar{z}) + \phi'$, $\alpha_d = \bar{\alpha}_d(\bar{z}) + \alpha_d'$, and $p_s = \bar{p}_s(x,y) + p_s'$ where the variables denoted by overbars are reference state variables that satisfy hydrostatic balance.

For completeness, the diagnostic relation for Ω is given by integrating Eq. (6) vertically from the surface ($\eta = 1$) to the material surface as

$$\Omega = -\int_1^\eta \left(\frac{\partial B(\eta)}{\partial \eta}\frac{\partial p_s'}{\partial t} + \nabla_\eta \cdot \vec{V}_H\right) d\eta, \quad (9)$$

where $\frac{\partial p_s'}{\partial t}$ is obtained by integrating vertically Eq. (6) for the surface ($\eta = 1$) to the top

($\eta = 0$) using a no-flux boundary condition such as $\Omega\big|_{\eta=0 \text{ or } 1} = 0$ and the specification of the vertical coordinate such as $B(\eta = 1) = 1$ and $B(\eta = 0) = 0$ as

$$\frac{\partial p_s'}{\partial t} = -\int_{\eta=0}^{\eta=1} \left(\nabla \cdot \vec{V}_H\right) d\eta . \tag{10}$$

The above equation allows p_s' to be evolved forward in time where we then compute μ_d' directly from Eq. (5). The diagnostic relation for the dry inverse density is given as

$$\frac{\partial \phi'}{\partial \eta} = -\bar{\mu}_d \alpha_d' - \alpha_d \mu_d' , \tag{11}$$

and the full pressure for dry atmosphere is

$$p = p_0 \left(\frac{R_d \theta}{p_0 \alpha_d} \right)^{c_p / c_v} . \tag{12}$$

This concludes the description of the governing equations used in our model; in the next section we describe the discretization of the continuous form of the governing equations that are used in our model.

3. Discretization

a. Spatial discretization

1) Horizontal direction

For a given η level, we discretize the horizontal operators using the SEM. Therefore in 2D (X-Z) slice framework we focus on the SEM discrete gradient operator for 1D (x). In SEM, we approximate the solution in non-overlapping elements Ω^e as

$$q(x,t) = \sum_{k=1}^{N+1} \psi_k(x) q_N(x_k, \mathrm{t}) , \tag{13}$$

where x_k represents $N+1$ grid points that correspond to the Gauss-Lobatto-Legendre (GLL) points and $\psi_k(x)$ are the N th-order Lagrange polynomials based on the GLL points.

153 It is noteworthy that the ψ_k have the cardinal property, i.e., they can be represented as
154 Kronecker delta functions where ψ_k are zero at all nodal points except x_k (but are
155 allowed to oscillate between nodal points).

156 The GLL points ξ_k in a reference coordinate system $\xi \in [-1,+1]$ and the associated
157 quadrature weights $\omega(\xi_k)$,

158 $$\omega(\xi_k) = \frac{2}{N(N+1)}\left[\frac{1}{P_N(\xi_k)}\right]^2, \tag{14}$$

159 are introduced for the Gaussian quadrature:

160 $$\int_{\Omega^e} q \; d\Omega^e = \int_{-1}^{+1} q(\xi)\left|J(\xi)\right| \, d\xi \approx \sum_{i=0}^{N} \omega(\xi_i) q(\xi_i)\left|J(\xi_i)\right|, \tag{15}$$

161 where $P_N(\xi)$ are the N th-order Legendre polynomials, $J = \frac{\partial x}{\partial \xi}$ is the transformation
162 Jacobian, and Ω^e represents the non-overlapping elements.

163 We now introduce the polynomial expansions into our governing equations in the form
164 of
$$\frac{\partial q}{\partial t} = -F(q), \tag{16}$$

165 multiply by the basis function as a test function, and integrate to yield a system of ordinary
166 differential equations as such

167 $$\sum_{n=1}^{N+1} M_{nk}^e \frac{dq_k}{dt} = -\int_{\Psi_e} F\left(\sum_{n=1}^{N+1} \psi_n(\xi) q_n\right) \psi_k \; d\xi, \tag{17}$$

168 where $k = 1, 2, \mathrm{L}\,, N+1$, M_{nk}^e is the element based mass matrix given as

169 $$M_{nk}^e = \int_{\Psi_e} \psi_n \psi_k \; d\xi = \omega_n \left|J_n\right| \delta_{nk}, \tag{18}$$

170 and the right-hand side of Eq. (18) is evaluated using Gaussian quadrature of Eq. (16). It is
171 noted that using GLL points for both interpolation and integration results in a diagonal mass

matrix M^e_{nk}, which means that the inversion of the mass matrix is trivial.

The horizontal derivatives included in the right-hand side of Eq. (17) are evaluated using the analytic derivatives of the basis functions as follows

$$\frac{\partial q}{\partial x} = \frac{\partial q}{\partial \xi}\frac{\partial \xi}{\partial x} = \frac{\partial}{\partial \xi}\left[\sum_{k=1}^{N+1} \psi_k(\xi) q_k\right]\frac{\partial \xi}{\partial x} = \left[\sum_{k=1}^{N+1} \frac{\partial \psi_k}{\partial \xi} q_k\right]\frac{1}{|J|}. \tag{19}$$

Note that the non-differential operations, such as cross products, are computed directly at grid points since we use nodal basis functions associated with Lagrange polynomials based on the GLL points. In order to satisfy the equations globally, we use the direct stiffness summation (DSS) operation. For a more detailed description of the SEM, see Giraldo and Rosmond (2004), Giraldo and Restelli (2008), and Kelly and Giraldo (2012).

2) Vertical direction

Using a Lorenz staggering, the variables $\vec{V}_H$, Θ, μ, α, p are at layer midpoints denoted by $k = 1, 2, \mathrm{K}, K$ where K is the total number of layers, and the variables W, Ω, ϕ live at layer interfaces defined by $k + \frac{1}{2}$, $k = 0, 1, \mathrm{K}, K$, so that $\eta_{K+1/2} = \eta_{top}$ and $\eta_{1/2} = \eta_{Bottom} = 1$. Fig. 1 describes the grid points and the allocation of the variables. Here, we evaluate the vertical advection terms ($\frac{\partial(\Omega \vec{V}_H)}{\partial \eta}$, $\frac{\partial(\Omega W)}{\partial \eta}$, and $\frac{\partial(\Omega \theta)}{\partial \eta}$) and vertical derivative terms ($\frac{\partial p'}{\partial \eta}$, and $\frac{\partial \phi}{\partial \eta}$). The former is discretized using the third-order upwind biased discretization in Hundsdorfer et al. (1995) which is given as

$$\left.\frac{\partial f}{\partial \eta}\right|_k = \frac{f_{k-2} - 8f_{k-1} + 8f_{k+1} - f_{k+2}}{12\Delta\eta} + \mathrm{sign}(\Omega)\frac{f_{k-2} - 4f_{k-1} + 6f_k - 4f_{k+1} + f_{k+2}}{12\Delta\eta}, \tag{20}$$

where f corresponds to the flux such as $\Omega \vec{V}_H$, and $\Delta\eta = \eta_{k+1/2} - \eta_{k-1/2}$ is the thickness of

the layer. The latter is discretized by the centered finite difference. Likewise the vertical discretization quadrature rules for the calculations of Eqs. (9) and (10) follow the finite difference discretization naturally.

b. Temporal discretization

For integrating the equations, we use the time-split RK3 integration technique following the strategy of SK08, in which low-frequency modes due to advective forcings are explicitly advanced using a large time step of the RK3 scheme, but high-frequency modes are integrated over smaller time steps using an explicit forward-backward time integration scheme for the horizontally propagating acoustic/gravity waves and a fully implicit scheme for vertically propagating acoustic waves and buoyancy oscillations (Klemp et al. 2007) . This technique has been shown to work effectively within numerous nonhydrostatic models including the WRF model (Skamarock et al. 2008), the Model for Prediction Across Scales (MPAS) (Skamarock et al. 2012), and the Nonhydrostatic Icosahedral Atmospheric Model (NICAM) (Satoh et al. 2008).

It is noted that in the procedure of the time-split RK3 integration, the difference between the approach used in this paper and SK08 comes from the vertical coordinate. Since we use the hybrid sigma-pressure coordinate, the equation for p'_s (Eq. (6)) should be first stepped forward in time using the forward-backward differencing on the small time steps, then μ'_d can be computed directly from the specification of the vertical coordinate in Eq. (9) and Ω is obtained from the vertical integration.

4. Test cases

We validate the 2DNH model on four test cases of the linear hydrostatic mountain wave,

density current, inertia-gravity wave, and rising thermal bubble experiments. All cases but the mountain wave experiment do not have analytic solutions. Therefore, for the mountain wave experiment, numerical results of the 2DNH model are compared to analytic solutions (Durran and Klemp 1983), and for the other experiments, we compare our results to the results of other published papers.

It should be mentioned that the horizontal SEM formulation is able to utilize arbitrary order polynomials per element to represent the discrete spatial operators, but in this paper all the results presented use either 5th or 8th order polynomials. The averaged horizontal grid spacing is defined as

$$\Delta\overline{x} = \frac{\sum_{n=1}^{N} \Delta x_n}{N} \tag{21}$$

where Δx_n is the internal grid spacing within the element which is regularly spaced in the domain and N is the number of the interval associated with irregularly spaced GLL quadrature points which is equivalent to the order of the basis polynomials. The average vertical grid spacing is defined in the same way of Eq. (24). Below, we use this convention to define the grid resolution.

a. Linear hydrostatic mountain wave test

In order to verify the 2DNH's feasibility to treat surface elevations associated with the vertical terrain-following coordinate, we simulate the linear hydrostatic mountain wave test introduced by Durran and Klemp (1983) (hereafter, DK83) in which the analytic steady-state solution is provided by using a single-peaked mountain with uniform zonal wind. To compare our results with the analytic and numerical solution shown in DK83, the 2DNH is initialized using the same initial conditions and mountain profile in DK83 and we analyze our results

239 using the same metrics of DK83.

240 The mountain profile is given by

241 $$h(x) = \frac{h_m}{1+\left(\frac{x - x_c}{a_m}\right)^2} \tag{22}$$

242 where the half-length of the mountain a_m is 10 km, the height h_m is 1 m, and the
243 prescribed center of the profile is 0 km. The Initial temperature is $T_0 = 250$ K for an
244 isothermal atmosphere with the uniform zonal wind $\bar{u} = 20$ m/s. In the isothermal case, the
245 Brunt-Väisälä frequency $N^2 = g\frac{d(\ln\bar{\theta})}{dz} \approx \frac{g^2}{c_p T_0}$ yields the potential temperature given as

246 $$\bar{\theta} = \theta_0 e^{\frac{g}{c_p T_0} z}, \tag{23}$$

247 which is one of the prognostic variables in our model. The domain is defined as
248 $(x,z) \in [-300,300] \times [0,30]$ km^2. The bottom boundary uses a no-flux boundary
249 condition while the lateral and top boundaries use sponge layers. The sponged zone is 10 km
250 deep from the top and 50 km wide from the lateral boundaries. Over the sponge layer zone,
251 the prognostic variables are relaxed to the basic initial hydrostatic state. The model is
252 integrated for a nondimensional time of $\frac{\bar{u}t}{a} = 60$ which corresponds to 8.33 hours without
253 diffusion or viscosity.

254 Fig. 2 shows the numerical and analytic solutions at steady state for the horizontal and
255 vertical velocities, which agree reasonably well. The vertical velocity fields match very
256 closely, although the extrema in the horizontal velocity field are underestimated by the
257 numerical model. The underestimated extrema in the horizontal velocity is also shown in both
258 models of DK83 and Giraldo and Restelli (2008) (hereafter, GR08). And our result in the

horizontal velocity is in good agreement with DK83 and GR08.

Fig. 3 shows the normalized momentum flux values at various times to check vertical transport of horizontal momentum. It is observed that the flux is developing well and the simulations have reached steady-state after $\frac{\bar{u}t}{a} = 60$. It is noted that the mean momentum flux at that time is 97% of its analytic value. It agrees well with DK83 as well as GR08; it is important to point out that the Durran-Klemp model is based on the FD method in both directions while the Giraldo-Restelli model is based on SEM in both directions. The mountain test shows the terrain-following vertical coordinate is well suited for the combination of the horizontal SEM and vertical FDM for spatial discretization even though we consider a small mountain.

b. 2D density current test

In order to verify the 2DNH's feasibility to control oscillations with numerical viscosity and evaluate numerical schemes in the 2DNH, we conduct the density current test suggested by Straka et al. (1993). The density current test is initialized using a cold bubble in a neutrally stratified atmosphere. When the bubble touches the ground, the density current wave starts to spread symmetrically in the horizontal direction forming Kelvin-Helmholtz rotors. Following Straka et al. (1993) we employ a dynamic viscosity of $\nu = 75$ $\mathrm{m^2 s^{-1}}$ to obtain converged numerical solutions.

For an initial cold bubble, the potential temperature perturbation is given as

$$\theta' = \frac{\theta_c}{2}\left[1+\cos(\pi r)\right], \tag{24}$$

where $\theta_c = -15$ K and $r = \sqrt{\left(\frac{x - x_c}{x_r}\right)^2 + \left(\frac{z - z_c}{z_r}\right)^2}$ with the center of the bubble at

281 $(x_c, z_c) = (0, 3000)$ m. No-flux boundary conditions are used for all boundaries. The model
282 is integrated for 900 s on a domain $[-25600, 25600] \times [0, 6400]$ m^2.

283 Fig. 4 shows the potential temperature perturbation after 900s for 400, 200, 100, and
284 50m grid spacing ($\Delta\bar{x}$) using 5th order basis polynomials per element. All simulations use
285 $\Delta\bar{z} = 64$ m grid spacing vertically. As expected, the higher resolution experiments produce
286 better solutions than the lower resolution. At the very lowest resolution of 400 m, only two of
287 the three Kelvin-Helmholtz rotors are generated with somewhat coarsened frontal surfaces. In
288 the experiment with 200 m resolution, the three rotors appear but the numerical solution still
289 suffers from coarsening frontal surfaces. The solutions on grids finer than 100 m converge
290 with the three rotor structures adequately simulated. The converged solution is almost
291 identical to other published solutions (e.g. Straka et al. 1993; Skamarock and Klemp 2008;
292 GR08).

293 In order to show the effect of higher order of the basis polynomials, we show the
294 potential temperature perturbations using 8th order basis polynomials per element with the
295 same number of degrees of freedom (DOF) of the simulations using 5th order basis
296 polynomials in Fig. 5. The simulation with 8th order basis polynomials on the very lowest
297 resolution of 400 m reproduced the converged solution more closely than with 5th order basis
298 polynomials. Even in the experiment with 200 m resolution, the coarsening frontal surfaces
299 are mitigated and the solution is similar with the converged solution with three rotors.

300 Fig. 6 shows the profiles of the potential temperature perturbation at the height of 1200
301 m. The results from the highest grid resolution of the simulations using 5th and 8th order
302 basis polynomials are indistinguishable and well converged (Fig. 6a). Three minima
303 corresponding to the three rotors agree well with other published solutions. In addition to the
304 profiles, the front location (-1K of potential temperature perturbation at the surface), and the

305 extrema of the pressure perturbation and potential temperature perturbation agree well with
306 each other (Table 1), of which the numbers are comparable to those of GR08. In the
307 numerical results from the different grid resolutions simulated by using 5th order basis
308 polynomials, the potential temperature profile at the coarsest resolution of 400 m grid shows
309 significant fluctuations (Fig. 6b). That of 8th order polynomials, however, tends to be
310 relieved from the deviation from the converged solution (Fig. 6c). The above results suggest
311 that the numerical solution can be converged more rapidly by using higher order of basis
312 polynomial. Furthermore, the results in this paper show that an adequate convergence can be
313 reached at grid resolutions finer than 200 m.
314
315 c. Inertia-gravity wave test
316 This test examines the evolution of a potential temperature perturbation θ' in a
317 constant mean flow with a stratified atmosphere. This initial perturbation diverges to the left
318 and right symmetrically in a channel with periodic lateral boundary conditions. The inertia-
319 gravity wave test introduced by Skamarock and Klemp (1994) (hereafter, SK94) serves as a
320 tool to investigate the accuracy for NH dynamics. Also we use this experiment to check the
321 consistency of the results with various resolutions. The parameters for the test are the same as
322 those of SK94. The initial state is a constant Brunt-Väisälä frequency of $N = 0.01$/s with
323 surface potential temperature of $\theta_0 = 300$ K and a uniform zonal wind $\bar{u} = 20$ m/s. In order
324 to trigger the wave, the initial potential temperature perturbation θ' is overlaid to the above
325 initial state and is given as

326 $$\theta'(x,z) = \theta_c \frac{\sin\left(\frac{\pi z}{z_c}\right)}{1+\left(\frac{x-x_c}{a_c}\right)} \tag{25}$$

where $\theta_c = 0.01$ K, $z_c = 10$ km, $x_c = 100$ km. The domain is defined as $(x,z) \in [0,300] \times [0,10]$ km^2. We use periodic lateral boundary conditions and a no-flux boundary conditions for both the bottom and top boundaries. The simulation is performed for 3000s with no viscosity.

Fig. 7 shows the solution θ' at the initial time and time 3000 s with a horizontal resolution $\Delta\bar{x} = 250$ m and a vertical resolution $\Delta\bar{z} = 250$ m. The figure uses the same contouring interval as in SK94 and Giraldo and Restelli (2008) for comparison. The results are produced with 8th order polynomials per element. We have conducted the 2DNH model with various basis polynomial orders at the same resolution, where the simulated results are found to be very comparable. SK94 give an analytic solution for the case of the Boussinesq equations, but it is only valid for the Boussinesq equations while we use the fully compressible equations in our model. Using the analytic solution only for qualitative comparisons, we find that the extrema of our results are comparable to the analytic values. In comparison with the results of Giraldo and Restelli (2008) in which the fully compressible equations are also used, our results look very similar. Fig. 8 shows the profiles along 5000 m for various horizontal resolutions. All models show consistently identical solutions with the symmetric distribution about the midpoint ($x = 160$ km) which is the location to which the initial perturbation moved by the horizontal flow of 20 m/s after 3000 s. Even at coarser resolution experiments, it does not exhibit phase errors although the maxima and minima near the midpoint ($x = 160$ km) are slightly damped. Table 2 shows the extrema of vertical velocities and potential temperature perturbations for the results of various horizontal resolutions after 3000 s. It is noted that all experiments give almost the same values for potential temperature perturbation where these values in the range $\theta' \in [-1.52 \times 10^{-3}, 2.83 \times 10^{-3}]$ are comparable to other studies (e.g., GR08 and Li et al.

2013). GR08 give the ranges of $\theta' \in \left[-1.51\times10^{-3}, 2.78\times10^{-3}\right]$ from the model based on the spectral element and discontinuous Galerkin method. Also Li et al. (2013) show $\theta' \in \left[-1.53\times10^{-3}, 2.80\times10^{-3}\right]$ using the high-order conservative finite volume model which are similar to our results.

d. Rising thermal bubble test

We also conduct the rising thermal bubble test to verify the consistency of the scheme in the model to simulate thermodynamic motion (Wicker and Skamarock 1998). This test considers the time evolution of warm air in a constant potential temperature environment for an atmosphere at rest atmosphere. The air that is warmer than the ambient air rises due to buoyant forcing which then deforms due to the shearing motion caused by gradients of the velocity field and eventually shapes the thermal bubble into a mushroom cloud. Because the test case has no analytic solution, the simulation results are evaluated qualitatively.

The initial conditions we use follow those of GR08 in which the domain for the case is defined as $(x,z) \in [0,1]^2$ km^2. We consider no-flux boundary conditions for all four boundaries. The domain is initialized for a neutral atmosphere at rest with $\theta_0 = 300$ K in hydrostatic balance. A potential temperature perturbation to drive the motion is given as

$$\theta' = \begin{cases} 0 & \text{for } r > r_c \\ \dfrac{\theta_c}{2}\left[1+\cos\left(\dfrac{\pi r}{r_c}\right)\right] & \text{for } r \le r_c \end{cases}, \tag{26}$$

where $\theta_c = 0.5$ K, $r = \sqrt{(x-x_c)^2 + (z-z_c)^2}$ with $(x_c, z_c) = (500, 350)$m. The model was run for a time of 700 seconds. It should be noted that an explicit second-order diffusion on coordinate surfaces is used with a viscosity coefficient of $\nu = 1$ m^{2}s^{-1} for all simulations

372 of this test. The numerical diffusion is applied for momentum and potential temperature along
373 the horizontal and vertical directions so that it eliminates the erroneous oscillations at the
374 small scale – while this amount of diffusion might seem excessive, it has been chosen
375 because it allows the model to remain stable even after the bubble hits the top boundary.

376 Fig. 9 shows the potential temperature perturbation, horizontal wind, and vertical wind
377 fields for the simulations of two resolutions of 20 m and 5 m horizontal and vertical grid
378 spacings ($\Delta\bar{x}$ and $\Delta\bar{z}$), respectively, employing 5th order basis polynomials. In both
379 simulations, the fine structures in the numerical solutions are well depicted with a perfectly
380 symmetric distribution at the midpoint and sharp discontinuities of the fields along boundary
381 lines of the bubble. At lower resolution, however, degradations in the solution are visible in
382 the potential temperature perturbation and vertical wind which are illustrated by fluctuations
383 in the values as well as the concaving contours at the top of the bubble. It is noted that while
384 the numerical solution of the model using the spatially centered FDM of Wicker and
385 Skamarock (1998) shows spurious oscillations in the potential temperature field, the
386 simulations here of 2DNH using the horizontally SEM and vertically FDM is devoid of these
387 oscillations.

388 We also show the vertical profiles of potential perturbation at x = 500 m after 700 s for
389 various resolutions in Fig. 10. Simulations were run with various resolutions of 5, 10, and 20
390 m, where the resolutions given are defined for both the horizontal and vertical directions. The
391 results of 10 m and 5 m resolutions are almost identical to each other. The result of the lowest
392 resolution of 20 m, however, shows a somewhat unresolved solution, in which the maximum
393 value is underestimated and the phase shift is depicted. The time series for maximum
394 potential temperature perturbation and maximum vertical velocity are shown in Fig. 11. In all
395 simulations, the maximum vertical velocity increases as the maximum theta perturbation
396 decreases. This shows that the thermal energy of the theta perturbation leads to the

acceleration of the vertical velocity. This result agrees well with the study of Ahmad and Lindeman (2007).

6. Summary and Conclusions

The non-hydrostatic compressible Euler equations for a dry atmosphere are solved in a simplified 2D slice (X-Z) framework by using the spectral element discretization (SEM) in the horizontal and the third-order finite difference scheme for the vertical discretization. The form of the Euler equations used here are the same as those used in the Weather Research and Forecasting (WRF) model. We employ a hybrid sigma-pressure vertical coordinate which can be modified exactly to the sigma-pressure coordinate at the level of the actual coding implementation.

For the spatial discretization, the spatial operators are separated into their horizontal and vertical components. In the horizontal components, the operators are discretized using the SEM in which high-order representations are constructed through the GLL grid points by Lagrange interpolations in the elements. Using GLL points for both interpolation and integration results in a diagonal mass matrix, which means that the inversion of the mass matrix is trivial. In the vertical components, the operators are discretized using the third-order upwind biased finite difference scheme for the vertical fluxes and centered differences for the vertical derivatives. The time discretization relies on the time-split third-order Runge-Kutta technique.

We have presented idealized standard benchmark tests for large-scale flows (e.g., linear hydrostatic mountain wave) and for nonhydrostatic-scale flows (e.g., inertia-gravity wave, rising thermal bubble, and density currents). The numerical results show that the present dynamical core is able to produce solutions of good quality comparable to other published

421 solutions. These tests effectively reveal that the combined spatial discretization method of the
422 spectral element and finite difference method in the horizontal and vertical directions,
423 respectively, offers a viable method for the development of a NH dynamical core. Further
424 research will be continued to couple the present core with the existing physics packages
425 together and extend the 2D slice framework to develop a 3D dynamical core for the global
426 atmosphere where the cubed-sphere grid will be used for the spherical geometry.
427

Acknowledgements

This work was funded by Korea's Numerical Weather Prediction Model Development Project approved by Ministry of Science, ICT and Future Planning (MSIP). The first author thanks Dr. Joseph B. Klemp for sharing his idea for the hybrid sigma-pressure coordinate, and would also like to thank Frank Giraldo for his assistance and his MA4245 course at Naval Postgraduate School which introduced us to the spectral element method. The second author gratefully acknowledges the support of KIAPS, the Office of Naval Research through program element PE-0602435N and the National Science Foundation (Division of Mathematical Sciences) through program element 121670.

References

Ahmad, N. and J. Lindeman, 2007: Euler solutions using flux-based wave decomposition. Int. J. Numer. Meth. Fluids, 54, 47-72.

Durran, D. R. and J. B. Klemp, 1983: A compressible model for the simulation of moist mountain waves. Mon. Wea. Rev., 111, 2341-2360.

Giraldo, F. X., 2001: A spectral element shallow water model on spherical geodesic grids. Int. J. Numer. Meth. Fluids, 35, 869–901.

Giraldo, F. X., and T. E. Rosmond, 2004: A Scalable Spectral Element Eulerian Atmospheric Model (SEE-AM) for NWP: Dynamical Core Tests. Mon. Wea. Rev., 132, 133-153.

Giraldo, F. X., 2005: Semi-implicit time-integrators for a scalable spectral element atmospheric model. Quart. J. Roy. Meteor. Soc., 131, 2431–2454.

Giraldo, F. X. and M. Restelli, 2008: A study of spectral element and discontinuous Galerkin methods for the Navier-Stokes equations in nonhydrostatic mesoscale atmospheric modeling: equation sets and test cases. Journal of computational physics 227, 3849-3877.

Giraldo, F. X., J. F. Kelly, and E. M. Constantinescu, 2013: Implicit-Explicit Formulations for a 3D Nonhydrostatic Unified Model of the Atmosphere (NUMA). SIAM J.

Sci. Comp. 35 (5), B1162-B1194.

Hundsdorfer, W., B. Koren, M. van Loon, and K. G. Verwer, 1995: A positive finite-difference advection scheme. Journal of Computational Physics, 117, 35-46.

Kelly, J. F. and F. X. Giraldo, 2012: Continuous and discontinuous Galerkin methods for a scalable three-dimensional nonhydrostatic atmospheric model: Limited-area mode. Journal of Computational Physics, 231, 7988–8008.

Klemp, J. B., W. C. Skamarock, and J. Dudhia, 2007: Conservative split-explicit time integration methods for the compressible nonhydrostatic equations. Mon. Wea. Rev., 135, 2897-2913.

Lauritzen, P., C. Jablonowski, M. Taylor, and R. Nair, 2010: Rotated versions of the Jablonowski steady-state and baroclinic wave test cases: A dynamical core intercomparison. J. Adv. Model. Earth Syst., 2. Art.#15.

Li, X., C. Chen, X. Shen, and F. Xiao, 2013: A multimoment constrained finite-volume model for nonhydrostatic atmospheric dynamics. Mon. Wea. Rev., 141, 1216-1240.

Park, S. –H., W. C. Skamarock, J. B. Klemp, L. D. Fowler, and M. G. Duda, 2013: Evaluation of global atmospheric solvers using extensions of the Jablonowski and Williamson baroclinic wave test case. Mon. Wea. Rev., 141, 3116-3129.

Satho, M., T. Matsuno, H. Tomita, H. Miura, T. Nasuno, and S. Iga, 2008: Nonhydrostatic icosahedral atmospheric model (NICAM) for global cloud resolving simulations. Journal of Computational Physics, 227, 3486-3514.

Skamarock, W. C. and J. B. Klemp, 1994: Efficiency and accuracy of the Klemp-Wilhelmson time-splitting technique. Mon. Wea. Rev., 122, 2623-2630.

Skamarock, W. C., J. B. Klemp, J. Dudhia, D. O. Gill, D. M. Barker, M. G. Duda, X. Y. Huang, W. Wang, and J. G. Powers, 2008: A desciption of the advanced research WRF version 3. NCAR Tech. Note TN-475+STR.

Skamarock, W. C. and J. B. Klemp, 2008: A time-split nonhydrostatic atmospheric model for weather research and forecasting applications. Journal of Computational Physics, 227, 3465-3485.

Skamarock, W. C. J. B. Klemp, M. G. Duda, L. D. Fowler, and S. –H. Park, 2012: A multiscale nonhydrostatic atmospheric model using centroidal Voronoi tessellations and C-grid staggering. Mon. Wea. Rev., 140, 3090-3105.

Straka, J. M., R. B. Wilhelmson, L. J. Wicker, J. R. Anderson, and K. K. Droegemeier, 1993: Numerical solutions of a non-linear density current: A benchmark solution and comparisons. Int. J. Numer. Methods Fluids, 17, 1-22.

514 Taylor, M., J. Tribbia, and M. Iskandarani, 1997: The spectral element method for the
515 shallow water equations on the sphere. Journal of computational physics 130,
516 92-108.
517
518 Taylor, M., J. Edwards, S. Thomas, and R. Nair, 2007: A mass and energy conserving
519 spectral element atmospheric dynamical core on the cubed-sphere grid. J. Phys.
520 Conf. Ser., 78(012074)
521
522 Thomas, S. J. and R. D. Loft, 2002: Semi-implicit spectral element atmospheric model.
523 Journal of Scientific Computing, 17, 339-350.
524
525 Thomas, S. J. and R. D. Loft, 2005: The NCAR spectral element climate dynamical core:
526 semi-implicit Eulerian formulation. Journal of scientific computing, 25, 307-
527 322.
528
529 Wicker, L. J. and W. C. Skamarock, 1998: A time-splitting scheme for the elastic equations
530 incorporating second-order Runge-Kutta time differencing. Mon. Wea. Rev.,
531 126, 1992-1999.
532

Table Captions

Table 1. Comparison between the 5th and 8th order polynomials per elements for the density current. The simulations is conducted with $\Delta\bar{x} = 50$ m and $\Delta\bar{z} = 50$ m resolution.

Table 2. Comparison of the numerical results for various horizontal resolutions. All simulations use the 8th order polynomials per elements and vertical resolution of $\Delta\bar{z} = 250$ m.

Table 1. Comparison between the 5th and 8th order polynomials per elements for the density current. The simulations is conducted with $\Delta\bar{x} = 50$ m and $\Delta\bar{z} = 50$ m resolution.

Order of polynomials	Front location(km)	p'_{max} (Pa)	p'_{min} (Pa)	θ'_{max} (K)	θ'_{min} (K)
5th	14.77	630.62	-452.79	0.08	-8.87
8th	14.74	626.91	-456.84	0.08	-8.94

Table 2. Comparison of the numerical results for various horizontal resolutions for inertia-gravity wave. All simulations use the 8th order polynomials per elements and vertical resolution of $\Delta\bar{z} = 250$ m.

Resolution(m)	w_{max} (m/s)	w_{min} (m/s)	θ'_{max} (K)	θ'_{min} (K)
$\Delta\bar{x} = 125$	2.85×10^{-3}	-2.89×10^{-3}	2.83×10^{-3}	-1.52×10^{-3}
$\Delta\bar{x} = 250$	2.80×10^{-3}	-2.82×10^{-3}	2.83×10^{-3}	-1.52×10^{-3}
$\Delta\bar{x} = 500$	2.73×10^{-3}	-2.73×10^{-3}	2.83×10^{-3}	-1.52×10^{-3}
$\Delta\bar{x} = 750$	2.72×10^{-3}	-2.70×10^{-3}	2.83×10^{-3}	-1.52×10^{-3}
$\Delta\bar{x} = 1250$	2.68×10^{-3}	-2.62×10^{-3}	2.82×10^{-3}	-1.52×10^{-3}

Figure Captions

FIG. 1. The grid points of columns within an element having four GLL points. The hybrid sigma coordinate are illustrated and the close (open) circles on the solid (dashed) line indicate the location of the variables at layer mid-points (interfaces).

FIG. 2. Steady-state flow of (left) horizontal velocity (m/s) and (right) vertical velocity (m/s) over 1 m high mountain at nondimensional time $\frac{\bar{u}t}{a} = 60$ with a grid resolution of $\Delta\bar{x} = 2$ km using 5th order basis polynomials per element and $\Delta\bar{z} = 375$ m. The numerical solution is represented by solid lines and the analytic solution by dashed lines.

FIG. 3. Vertical flux of horizontal momentum, normalized by its analytic value at several non-dimensional times $\frac{\bar{u}t}{a}$. Here M and M_H are the momentum flux of the numerical and analytic solution.

FIG. 4. Potential temperature perturbation after 900 s using (a) $\Delta\bar{x} = 400$ m, (b) $\Delta\bar{x} = 200$ m, (c) $\Delta\bar{x} = 100$ m, and (d) $\Delta\bar{x} = 50$ m grid spacing with 5th order basis polynomials per element. All simulations use $\Delta\bar{z} = 64$ m grid spacing.

FIG. 5. As in Fig. 4, but with 8th order basis polynomials per element.

FIG. 6. Profiles of potential temperature perturbation after 900 s along 1200 m height: (a) high-resolution simulations using 5th (thin solid line) and 8th (thick solid line) order basis function, (b) simulations using 5th order basis polynomials, and (c) simulations using 8th

573 order basis polynomials per element. Total number of the degrees of freedom is the same in
574 both 5th and 8th order experiments. All simulations use $\Delta\bar{z} = 64$ m grid spacing.
575
576 FIG. 7. Potential temperature perturbation at the initial time (left) and time 3000s (right)
577 for $\Delta\bar{x} = 250$ m using 8th order basis polynomials per element and $\Delta\bar{z} = 250$ m.
578
579 FIG. 8. The profiles of potential temperature perturbation along 5000 m height for
580 $\Delta\bar{x} = 125$ m (thick solid line), $\Delta\bar{x} = 500$ m (thin dashed line) and $\Delta\bar{x} = 1250$ m (thin
581 solid line) using 8th order basis polynomials per element. All models use $\Delta\bar{z} = 250$ m.
582
583 FIG. 9. Plots of (a,b) potential temperature perturbation (K), (c,d) horizontal wind (m/s),
584 and (e,f) vertical wind (m/s) for the rising thermal bubble test after 700s with (left)
585 $\Delta\bar{x} = 20$ m and (right) $\Delta\bar{x} = 5$ m resolution. All simulations use 5th order basis polynomials
586 per element and $\Delta\bar{z} = 10$ m grid spacing. All negative values are denoted by dashed lines
587 and positive values by solid lines.
588
589 FIG. 10. Vertical profiles of the potential temperature perturbation at x = 500 m after
590 700 s for various resolutions: $\Delta\bar{x}, \Delta\bar{z} = 20$ m (thin solid line), $\Delta\bar{x}, \Delta\bar{z} = 10$ m (thin dashed
591 line), and $\Delta\bar{x}, \Delta\bar{z} = 5$ m (thick solid line).
592
593 FIG. 11. (top) Domain maximum potential temperature perturbation and (bottom)
594 vertical wind for the rising thermal bubble test. All simulations use the 5th order basis
595 polynomials per element, and the vertical resolutions are the same as the horizontal
596 resolutions.
597

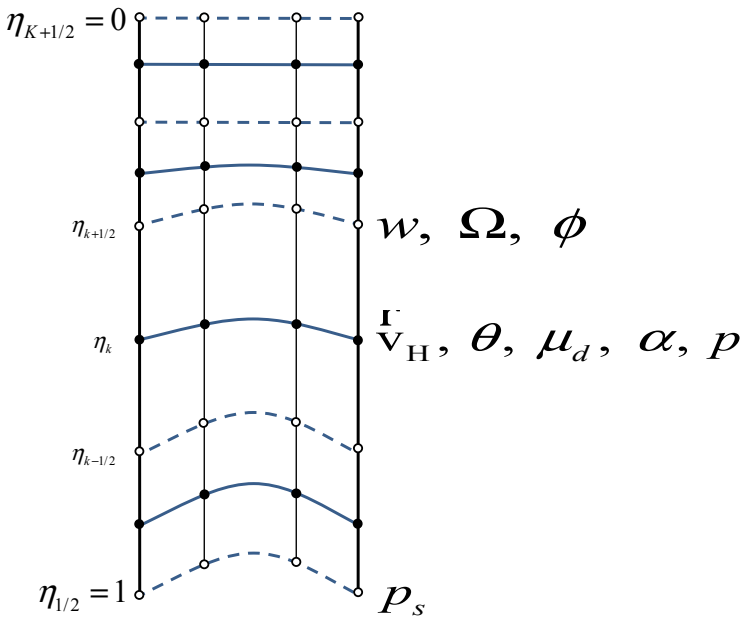

598

599 FIG. 1. The grid points of columns within an element having four GLL points. The
600 hybrid sigma coordinate are illustrated and the close (open) circles on the solid (dashed) line
601 indicate the location of the variables at layer mid-points (interfaces).

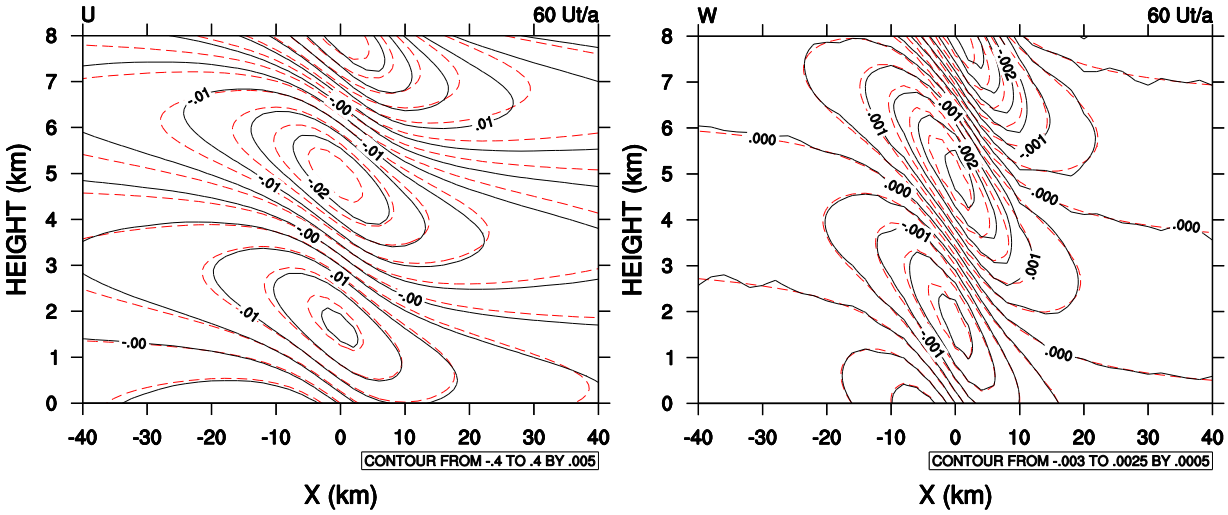

602

603 FIG. 2. Steady-state flow of (left) horizontal velocity (m/s) and (right) vertical velocity

604 (m/s) over 1 m high mountain at nondimensional time $\frac{\bar{u}t}{a} = 60$ with a grid resolution of

605 $\Delta\bar{x} = 2$ km using 5th order basis polynomials per element and $\Delta\bar{z} = 375$ m. The

606 numerical solution is represented by solid lines and the analytic solution by dashed lines.

607

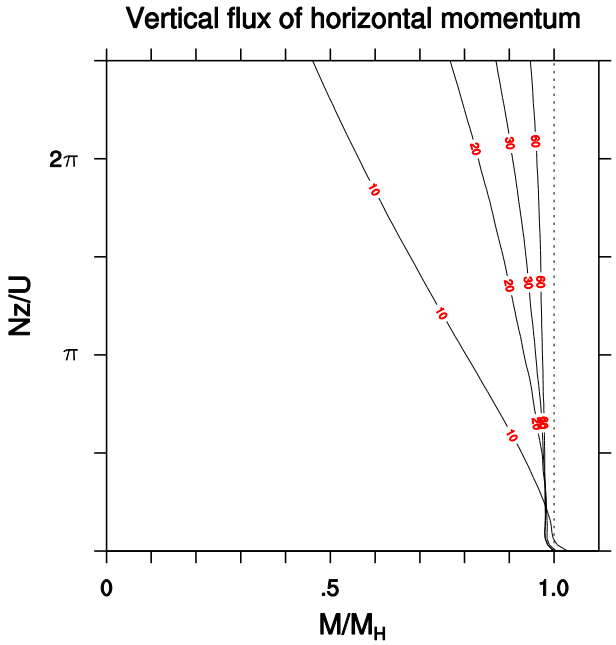

608

609 FIG. 3. Vertical flux of horizontal momentum, normalized by its analytic value at

610 several non-dimensional times $\frac{\bar{u}t}{a}$. Here M and M_H are the momentum flux of the numerical

611 and analytic solutions.

612

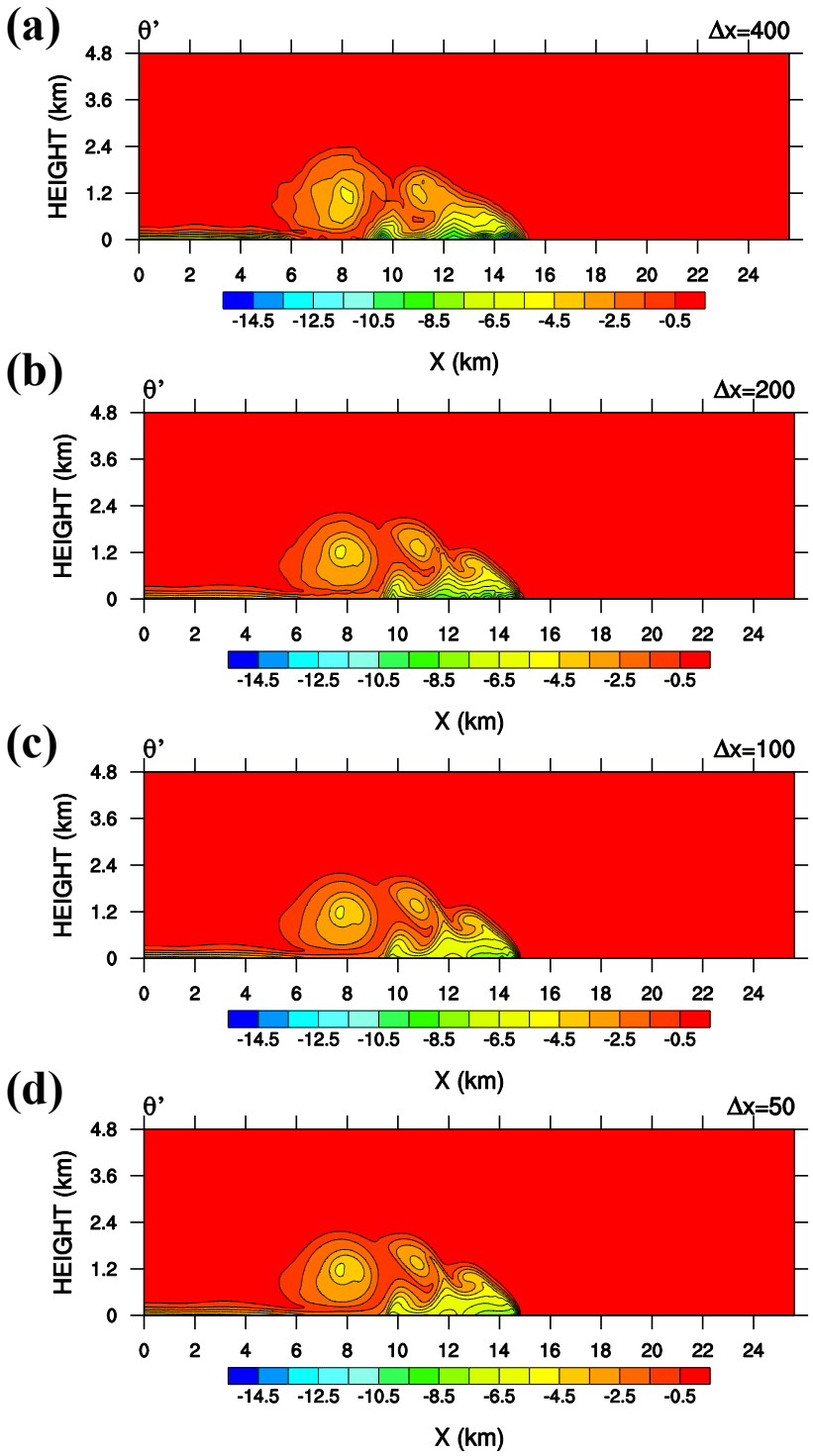

FIG. 4. Potential temperature perturbation after 900 s using (a) $\Delta\bar{x} = 400$ m, (b) $\Delta\bar{x} = 200$ m, (c) $\Delta\bar{x} = 100$ m, and (d) $\Delta\bar{x} = 50$ m grid spacing with 5th order basis polynomials per element for the density current. All simulations use $\Delta\bar{z} = 64$ m grid spacing.

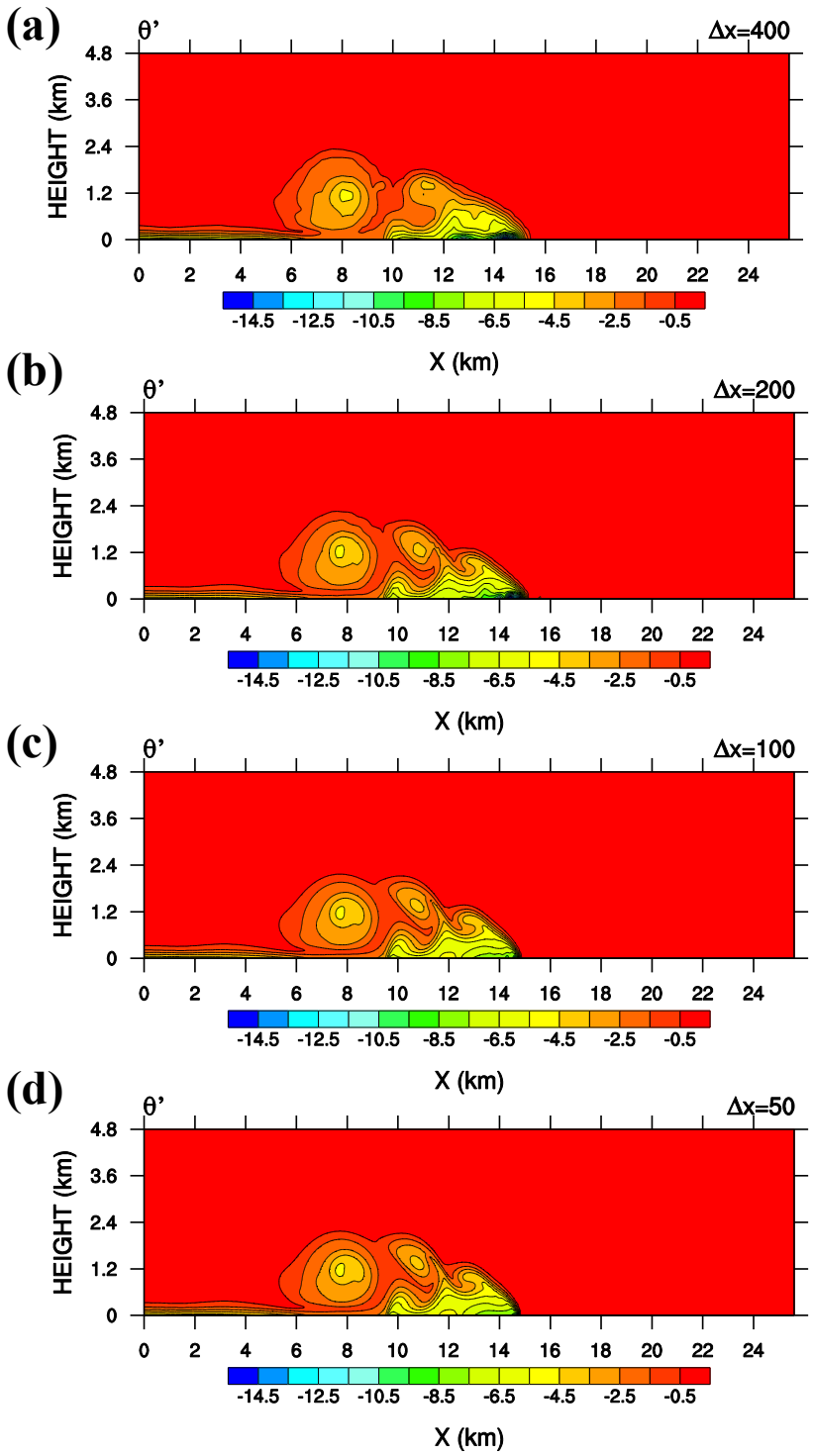

619

620 FIG. 5. As in Fig. 4, but with 8th order basis polynomials per element.

621

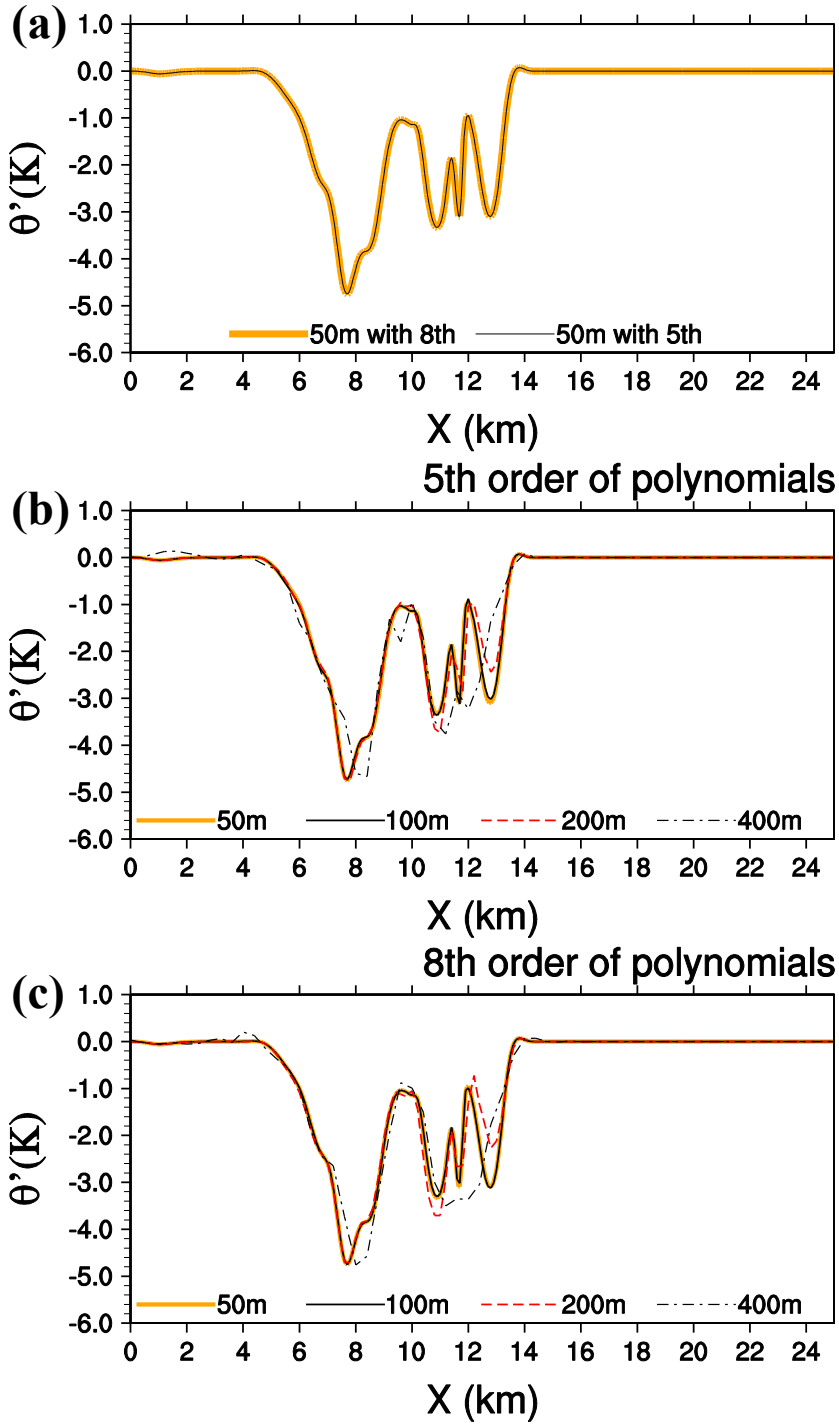

622

623 FIG. 6. Profiles of potential temperature perturbation after 900 s along 1200 m height:
624 (a) high-resolution simulations using 5th (thin solid line) and 8th (thick solid line) order basis
625 function, (b) simulations using 5th order basis polynomials, and (c) simulations using 8th
626 order basis polynomials per element. The total number of the degrees of freedom is the same
627 in both 5th and 8th order experiments. All simulations use $\Delta\bar{z} = 64$ m grid spacing.

628

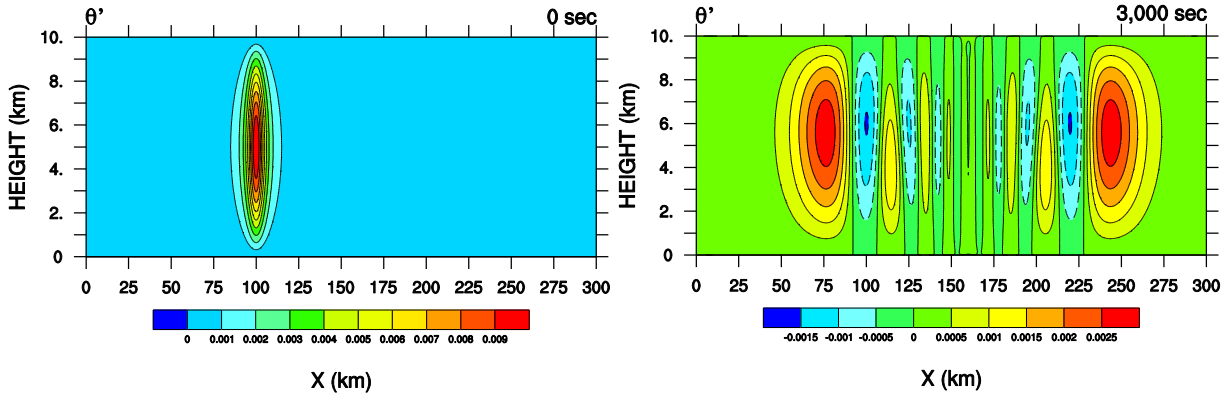

629

630 FIG. 7. Potential temperature perturbation at the initial time (left) and time 3000s (right)

631 for $\Delta\bar{x} = 250$ m using 8th order basis polynomials per element and $\Delta\bar{z} = 250$ m for the

632 inertia-gravity wave.

633

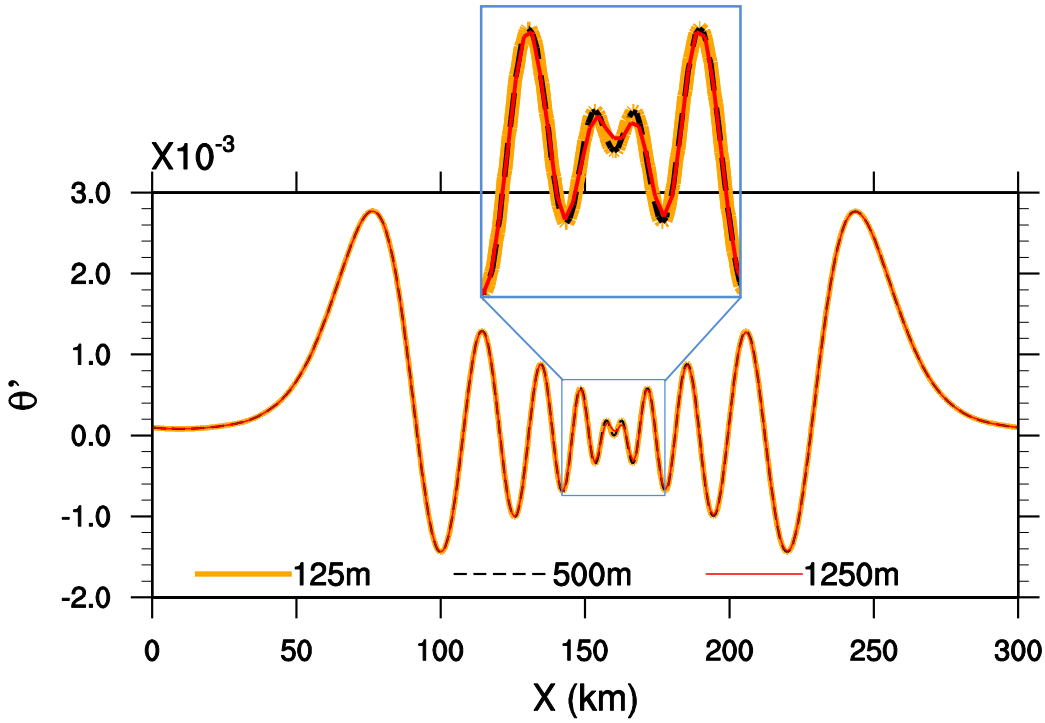

634

635 FIG. 8. The profiles of potential temperature perturbation along 5000 m height for
636 $\Delta\bar{x} = 125$ m (thick solid line), $\Delta\bar{x} = 500$ m (thin dashed line) and $\Delta\bar{x} = 1250$ m (thin
637 solid line) using 8th order basis polynomials per element for the inertia-gravity wave. All
638 models use $\Delta\bar{z} = 250$ m.

639

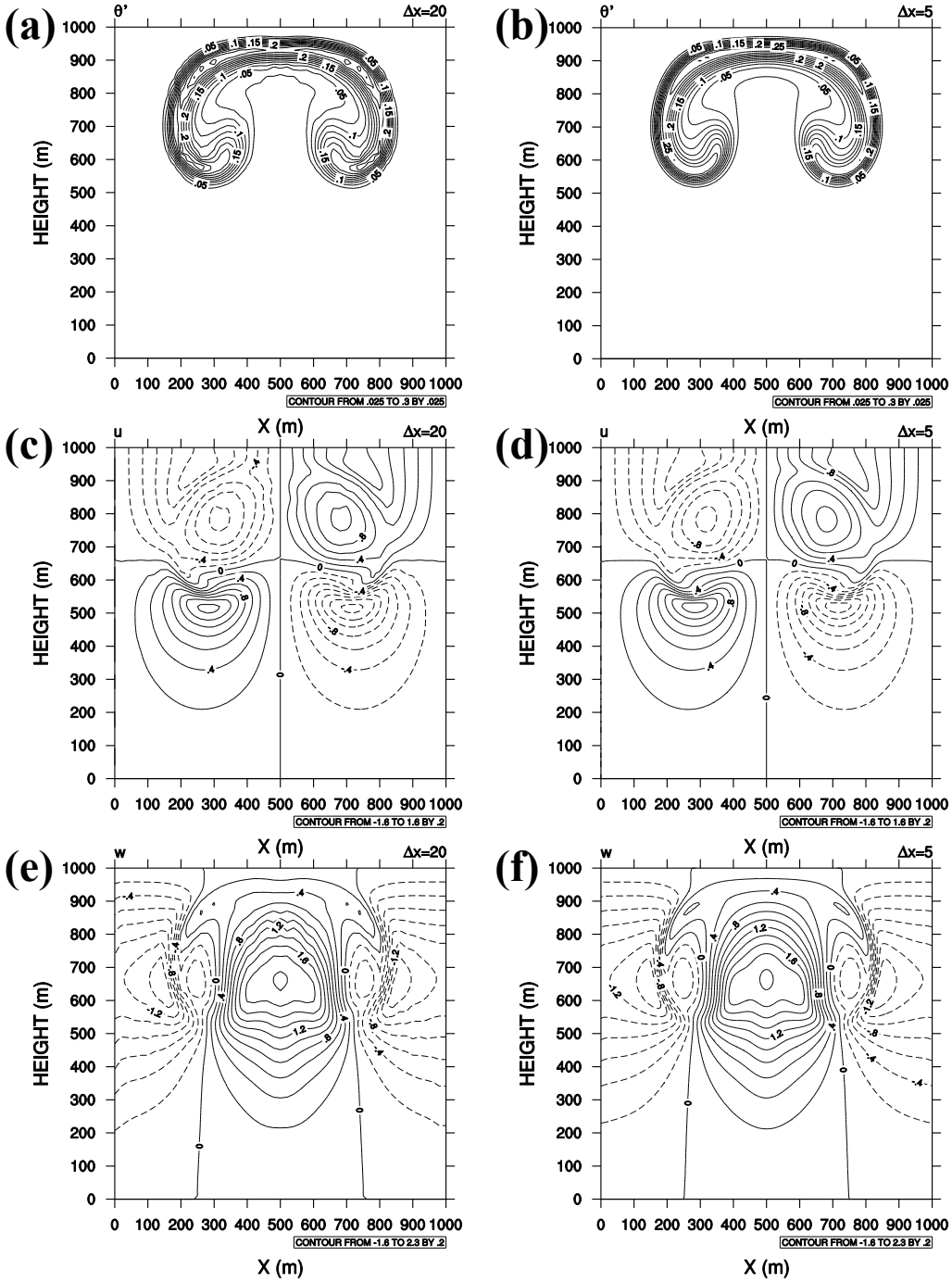

640

641 FIG. 9. Plots of (a,b) potential temperature perturbation (K), (c,d) horizontal wind (m/s),
642 and (e,f) vertical wind (m/s) for the rising thermal bubble test after 700s with (left)
643 $\Delta\bar{x}, \Delta\bar{z} = 20\,\text{m}$ and (right) $\Delta\bar{x}, \Delta\bar{z} = 5\,\text{m}$ resolution for the rising thermal bubble test. All
644 simulations use 5th order basis polynomials per element. All negative values are denoted by
645 dashed lines and positive values by solid lines.

646

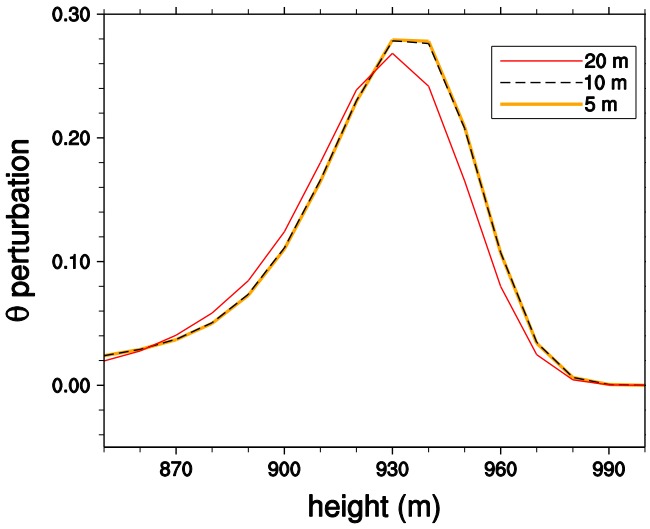

FIG. 10. Vertical profiles of the potential temperature perturbation for the rising thermal bubble test at x = 500 m after 700 s for various resolutions: $\Delta\bar{x}, \Delta\bar{z} = 20$ m (thin solid line), $\Delta\bar{x}, \Delta\bar{z} = 10$ m (thin dashed line), and $\Delta\bar{x}, \Delta\bar{z} = 5$ m (thick solid line).

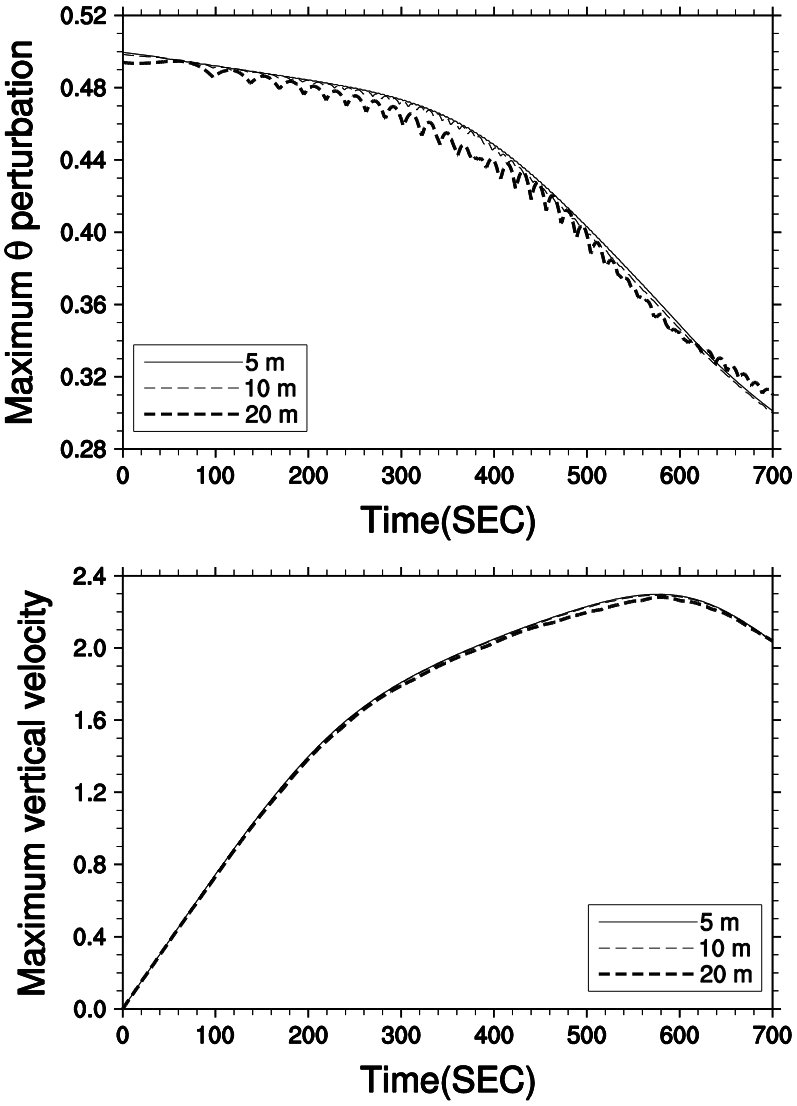

653

654 FIG. 11. (top) Domain maximum potential temperature perturbation and (bottom)
655 vertical wind for the rising thermal bubble test. All simulations use the 5th order basis
656 polynomials per element, and the vertical resolutions are the same as the horizontal
657 resolutions.